

Article

South Atlantic Surface Boundary Current System during the Last Millennium in the CESM-LME: The Medieval Climate Anomaly and Little Ice Age

Fernanda Marcello ^{1,*} , Ilana Wainer ¹ , Peter R. Gent ², Bette L. Otto-Bliesner ² and Esther C. Brady ²

¹ Department of Physical Oceanography, Oceanographic Institute of the University of São Paulo, São Paulo 05508-120, Brazil

² National Center for Atmospheric Research, Boulder, CO 80307, USA

* Correspondence: fernanda.marcello@usp.br

Received: 16 May 2019; Accepted: 3 July 2019; Published: 9 July 2019



Abstract: Interocean waters that are carried northward through South Atlantic surface boundary currents get meridionally split between two large-scale systems when meeting the South American coast at the western subtropical portion of the basin. This distribution of the zonal flow along the coast is investigated during the Last Millennium, when natural forcing was key to establish climate variability. Of particular interest are the changes between the contrasting periods of the Medieval Climate Anomaly (MCA) and the Little Ice Age (LIA). The investigation is conducted with the simulation results from the Community Earth System Model Last Millennium Ensemble (CESM-LME). It is found that the subtropical South Atlantic circulation pattern differs substantially between these natural climatic extremes, especially at the northern boundary of the subtropical gyre, where the westward-flowing southern branch of the South Equatorial Current (sSEC) bifurcates off the South American coast, originating the equatorward-flowing North Brazil Undercurrent (NBUC) and the poleward Brazil Current (BC). It is shown that during the MCA, a weaker anti-cyclonic subtropical gyre circulation took place (inferred from decreased southern sSEC and BC transports), while the equatorward transport of the Meridional Overturning Circulation return flow was increased (intensified northern sSEC and NBUC). The opposite scenario occurs during the LIA: a more vigorous subtropical gyre circulation with decreased northward transport.

Keywords: equatorial current bifurcation; western boundary currents; South Atlantic Subtropical Gyre; Meridional Overturning Circulation; Last Millennium; Medieval Climate Anomaly; Little Ice Age

1. Introduction

The South Atlantic Ocean (SAO) is unique in its establishment of teleconnections between the adjacent ocean basins and as a critical crossroads for the global Meridional Overturning Circulation (MOC) (e.g., [1]). A mixture of Pacific and Indian Ocean contributions is received at the southern opposing corners of the SAO basin, through the Drake Passage (the cold-water route, [2]) and the Agulhas Leakage (the so-called warm-water route, [3]). These are blended together and incorporated within the large-scale South Atlantic Subtropical Gyre (SASG) circulation to then continue to the northward flowing upper-limb of the MOC.

More specifically, waters from the cold-water route at the southwestern corner follow the South Atlantic Current (SAC) path to the east where they meet the warm-water route at the southern tip of Africa. From thereon, these interocean waters begin their course of northward advection, carried

by the Benguela Current (BeC) at the eastern boundary of the SASG, which smoothly turns into the southern branch of the South Equatorial Current (sSEC), delimiting the subtropical gyre to the north.

The sSEC heads westward crossing the basin until meeting the South American (SA) coast. At this point, the zonal flow gets divided meridionally between two important large-scale circulation systems. This is accomplished through the origins of two opposing western boundary currents (WBCs): the poleward Brazil Current (BC), closing the subtropical gyre circulation, and the equatorward North Brazil Undercurrent (NBUC), continuing to the upper ocean return flow of the MOC [4–6]. The sSEC-NBUC system is also the main conduit for the subtropical-tropical mass exchange [7–9].

The sSEC bifurcation occurs around 15° S at the surface [10,11]. As it moves southward, the NBUC transport increases and the BC transport decreases; while as it moves northward, the NBUC transport decreases and the BC transport increases [12]. Therefore, the sSEC bifurcation latitude (SBL) is indicative of how much subtropical water flows equatorward into the tropical/equatorial region via the NBUC and how much flows poleward, recirculating in the subtropical gyre via the BC.

It is suggested that the SBL, SASG, and Atlantic MOC (AMOC) dynamics have been and will continue to be significantly affected by increasing greenhouse gas concentrations in the 21st Century: model simulation results point to a southward shift of the SBL accompanied by an increase in the northward NBUC transport [13], while instrumental data show a current state of reduced overturning for the AMOC [14]. To better understand what portion of the latest variations might be actually attributable to external forcings and what reflects internal variability, it is crucial to place the modern climate warming in a longer term context [15,16].

The Last Millennium (LM) spans the most recent past before anthropogenic forcing became significant, representing an ideal opportunity to understand how the climate system varied under natural conditions [17,18]. It is marked by two significant climatic events resulting from natural variability: the Medieval Climate Anomaly (MCA) and the Little Ice Age (LIA). The MCA is generally considered to be a period of above-average temperatures for the years from 950–1249, while the LIA is a period of below-average temperatures from 1400–1699. We use here the definitions of Mann et al. [19] for each 300-year period.

A Note on MCA and LIA Conventions and Origins

One should keep in mind that “MCA and LIA” are regarded as the outstanding extremes of a simplistic picture of past global-scale climate variability [20]. There is no consensus of globally-/hemispherically-synchronous MCA and LIA periods [19,21,22], since specific timing of peak warm/cold intervals varies regionally [23]. Considering MCA/LIA spatio-temporal heterogeneity, it is recommended that the general use of such terms is complemented with specific calendar dates, as we have adopted those of Mann et al. [19].

When addressing possible causes of these major LM surface temperature anomalies, reconstructions show that the MCA and LIA are both distinct with regard to estimated external radiative forcing of the climate [20,24]. Nevertheless, studies have increasingly pointed to a combination of changes in external forcings with an important role played by internal climate variability [22,25–31].

The MCA pattern is based on a smaller number of predictors compared to the LIA pattern [19]. Still, there is indeed evidence of medieval warmth [32], although it is not geographically uniform when compared to the recent warming [22]. Besides relating to weaker volcanic eruptions and higher solar activity [33], the MCA-warmth is unlikely to have arisen as a response to external forcing alone. Past studies suggest that solar irradiance changes might have been amplified by internal Earth system feedbacks [22,34–36].

The LIA origins are also associated with external forcings including changes in orbital parameters and weaker solar activity, in turn [21,37], but more directly to consecutive pulses of volcanism [38], which also might have ended up driving internal climate feedbacks [39]. Proxies and climate modeling

efforts estimate that the MCA-LIA difference in global mean surface temperatures was close to 0.24 °C [19].

The histories of external forcings are not known precisely for the LM, as expected, but they must be imperfectly reconstructed from proxy information sources [20]. That said, there are substantial uncertainties in these reconstructed forcing factors, associated with dating, calibration and specific spatial patterns that are provided for the forcings when these are assimilated into global climate models. These need to be accounted for when interpreting any records and/or model-derived simulations in climate change attribution studies [40,41].

For the North Atlantic Ocean, it has been suggested from proxy evidence the occurrence of an enhanced AMOC during the MCA [42], followed by a weakened AMOC along the MCA/LIA transition [43]. Furthermore, using oxygen isotopes and Mg/Ca in fossil shells of planktonic foraminifera from high-resolution sediment cores, Lund et al. [44] showed a weaker Gulf Stream transport through the Florida Strait during the LIA. Nevertheless, for the upstream flow of the northward upper limb of the AMOC, there is little or no information on its variations during the LM.

In fact, there is little evidence from proxy data of South Atlantic circulation and dynamics, during either the MCA or the LIA. This can be noted, for instance, when observing the spatial distribution of surface temperature data over the SAO in Mann et al. [19] or Neukom et al. [45]. Furthermore, Graham et al. [32] discussed available proxy data for the MCA-LIA period and mentioned a range of studies that showed changes relative to the MCA and LIA for several regions, but not the SAO. Therefore, the behavior of the SAO circulation for the MCA-LIA period is largely unknown. To compensate for this, fully-coupled circulation models allow more detailed examinations of the spatial and temporal variations during the LM in comparison to the proxy data [46].

This study describes the western SAO surface boundary current system response to the naturally-forced events of the MCA and LIA. To do so, simulation results from the Community Earth System Model Last Millennium Ensemble (CESM-LME) experiment are examined [41]. We focus on the north-south distribution of the westward flow towards the SA coast, which is fed by the BeC at the eastern boundary of the subtropical gyre. As these waters turn westward, they are broadly spread across the basin and bifurcate. The sSEC bifurcation region marks the point from where interocean waters get divided between two important large-scale features: the SASG and the upper limb of the AMOC.

The divergence of the sSEC and resulting SASG/AMOC split of interocean waters are the primary motivation of this study. The ultimate goal is to evaluate and characterize the South Atlantic WBC system response to anomalously warm and cold periods of the LM: the MCA and LIA. Given that the WBC system in the SAO encompasses the SASG, as well as the AMOC, better understanding of the north-south distribution of the sSEC flow can give us insights into the dynamics of both of these circulation regimes. Moreover, the climate variability over the LM provides the essential context for assessing future changes [21].

This work is organized as follows. Section 2 provides a brief description of the model data used and methods. Section 3 presents the model simulation results regarding the MCA/LIA anomalous fields of the sea surface temperature (SST), horizontal velocities (UVEL, VVEL), and wind stress curl (WSC). The SST anomalies clearly characterize the contrasting conditions of the MCA and LIA periods (Section 3.1); the horizontal velocities (Section 3.2) are first described in terms of the mean circulation field (Section 3.2.1), then analyzed with regard to the MCA/LIA anomalous flows (Section 3.2.2); and the WSC anomalies emphasize the observed changes in the circulation pattern (Section 3.3). Section 4 summarizes and discusses the results and conclusions. Finally, a list of major acronyms is also included at the end of Section 4.

2. Data and Methods

The CESM-LME experiment included a set of simulations forced with reconstructions for the transient evolution of solar intensity, volcanic emissions, greenhouse gases, aerosols, land use/land

cover, and orbital parameters, both together and individually, for the period of 850–2006. Output from the ensemble members are available through the Earth System Grid (<http://www.earthsystemgrid.org>) as single-variable time series.

This study examined the ensemble-mean of 10 members with the full-set of external forcings to investigate the period of 850–1849. Monthly outputs were used.

The forcings were applied identically across ensemble members. The only difference among these experiments was the application of a random round-off difference in the air temperature field that initialized each experiment, which would eventually result in ensemble spread. For more details, the reader is referred to the overview paper of the Last Millennium Ensemble Project (Otto-Bliesner et al. [41]).

The CESM-LME used a 2-degree nominal resolution in the atmosphere and land components and a 1-degree nominal resolution in the ocean and sea ice components. The CESM 1.1 version used in this experiment was fully documented in [47]. Details on the ocean model, which has 60 vertical levels, were described in [48].

Results from the CESM-LME were recently employed in a wide range of climate variability studies [49–56], which extensively tested the model results against other Earth System Models of the CMIP5 [57] and also showed that the full-forcing realizations reproduced major modes of observed internal climate variability [46,58–60]. Figure S2, Table S1 and Table S2 in the Supplementary Material file show a comparison previously made between the CESM-LME, the ocean component of the CESM (the Parallel Ocean Program Version 2), and five ocean reanalysis products for mean SBL values.

Here, LM-mean defines the mean 850–1849 millennia period, and the 300-year MCA-mean and LIA-mean refer to the mean 950–1249 and 1400–1699 periods, respectively. The MCA-anomalies and LIA-anomalies were defined with respect to the whole LM period.

To explore variations in the wind-driven, upper ocean circulation associated with the SASG and the upper-limb return flow of the AMOC, depth integrated horizontal velocities above 200 m were used. This layer better reflects the variability of the WSC field and SSTs, also analyzed here. The large-scale WSC is considered a major forcing mechanism of the upper ocean [61], while SSTs strongly affect ocean-atmosphere coupling and therefore respond to the mean upper ocean circulation. Extending our analyses to deeper layers did not change our conclusions significantly.

3. Results

3.1. Sea Surface Temperature Field

The MCA and LIA SST anomalies are shown in Figure 1a,b, respectively. As indicated by the dashed contours, the LM-mean SST field was characterized by warmer waters at the tropical region, decreasing nearly exponentially towards higher latitudes, as expected. The MCA-mean SST for the region of study was 14.36 °C, while the LIA-mean SST was 14.25 °C, yielding a MCA-LIA SST difference of ~0.11 °C.

The MCA and LIA anomalous SST fields presented in Figure 1 had a similar spatial distribution, which were opposite in sign. However, the MCA-warming reached a greater amplitude (maximum of +0.17 °C at 57° W, 44° S) than the LIA-cooling (maximum cooling of –0.08 °C at 22° W, 45° S) for this region. The most remarkable differences were concentrated at the southern limits of the domain, where the maximum MCA-warming lied south of the mean-location of the Brazil-Malvinas Confluence (BMC), and the maximum LIA-cooling was located further east, towards the middle of the basin, where there is a region of amplified cooling spreading zonally and northwestwardly.

The spatial pattern of the SST anomalies in Figure 1a,b imply that, during the MCA, a region of higher SST anomalies occurred starting at the southeastern interior basin, between 10° W and 10° E, crossing the subtropical SAO, and extending toward the SA coast within the 10°–20° S latitudinal band. These hook-like anomalies characterize the BeC-sSEC path, covering the eastern and northern boundaries of the subtropical gyre. For the LIA period, this same hook-like anomalous feature did not evolve past the eastern portion of the basin, indicating that the cooling remained more confined to

the subtropical region, instead of extending up to the western boundary and the equatorial region, compared to the MCA anomalous pattern. The BC region south of $\sim 25^\circ$ S has higher-amplitude anomalies than in the MCA picture (which actually has its lower-amplitude fish-like blob of anomalies centered at this region). This points to more anomalies being advected south during the LIA and to the north during the MCA.

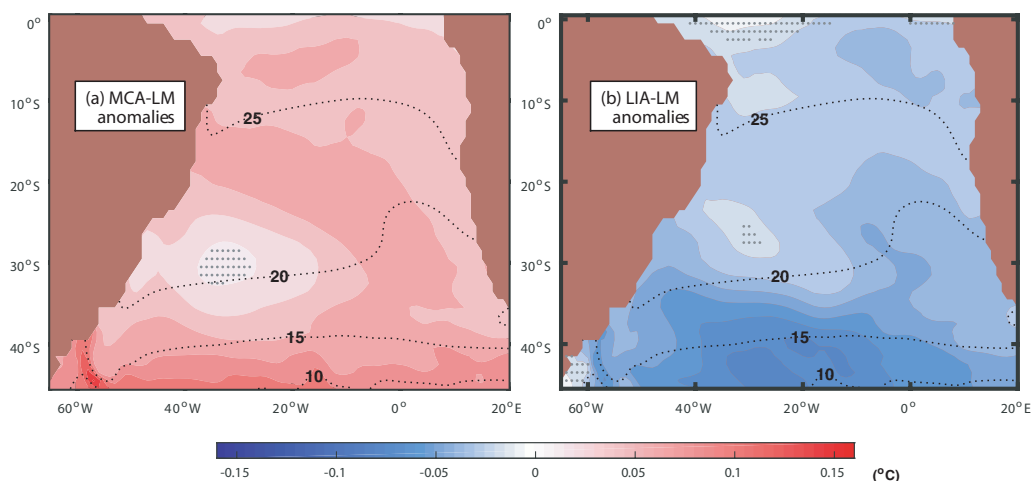


Figure 1. Sea surface temperature anomalies ($^{\circ}\text{C}$) with respect to the whole Last Millennium (LM) base period (850–1849). (a) For the Medieval Climate Anomaly (MCA), between 950 and 1249, and (b) for the Little Ice Age (LIA), between 1400 and 1699. The black dashed contours represent the LM-mean SST values, for reference. Red (blue) colors represent positive (negative) anomalies. Gray hatched areas indicate non-significant MCA/LIA-LM anomalies according to a two-sided t -test ($p < 0.05$).

In fact, anomalous signals lying at the southern boundary of the subtropical gyre tend to follow its anti-cyclonic circulation, being transported northwestward toward the SA coast and then distributed between the northern and southern circulation regimes. The observed MCA/LIA anomalous SST pattern suggests that the course of the northward advection started by the BeC at the southeastern SAO corner joined primarily the northward AMOC upper limb during the MCA, while during the LIA, it contributed mostly to the SASG, by bending southward after the bifurcation.

Our results presented virtually mirrored MCA/LIA SST anomalies, based on their similar spatial distribution, which was opposite in sign. These allowed us to assess the SA circulation system response to past extreme warm/cold climatic conditions, regardless of their distinct causes when compared to modern climate change (as discussed in Section 1).

3.2. Horizontal Velocity Field and Volume Transports

3.2.1. LM-Mean Circulation Field

The mean SAO upper 200-m circulation field within the region of study was well reproduced by the simulation results of the CESM-LME, according to existing literature [10,62–65] (Figure S1).

Background shading in Figure 2a represents the LM-mean meridional velocity field. To the east of the domain, it depicts the overall southward (blue) and northward (red) interior flows. These mark the division between the complex equatorial current system to the north (blue) and the anticyclonic subtropical circulation to the south (red). To the west of the domain, the narrow path of the opposing WBCs along the South American coast is clear. The superposed vectors indicate the LM-mean horizontal velocities (meridional, as well as zonal velocities). The black contour is the zero meridional velocity line, and the black dot represents the LM-mean SBL at the surface (25 m), as the point where the meridional velocity averaged within a 4° longitude band off the SA coast is zero.

The LM-mean zonal velocity for this region (Figure 2b) reveals a predominantly westward flow across the interior basin (blue) towards the western boundary, with the exception of a narrow eastward band close to the equator (red, north of $\sim 3^{\circ}$ – 4° S) which represents the Equatorial Undercurrent (EUC). The zonal upper 200-m currents are identified according to the schematic representation from Stramma and England [10] (Figure S1). Before it crosses the basin toward the SA coast, the sSEC supplies the eastward flow of the South Equatorial Countercurrent (SECC), which partially recirculates in the central branch of the South Equatorial Current (cSEC). The cSEC partially feeds the South Equatorial Undercurrent (SEUC) to the east, which heads toward the northern limit of the cyclonic Angola Gyre, further east of the domain (not shown). The cSEC then flows across the basin and provides a contribution to the western boundary. North of that is the southwestern flowing equatorial branch of the South Equatorial Current (eSEC), which branches out of the eastward flowing Equatorial Undercurrent (EUC) at the northern limit of the domain. Eastward and westward velocities along the coastline represent the spread of the WBCs formed north and south of the mean sSEC.

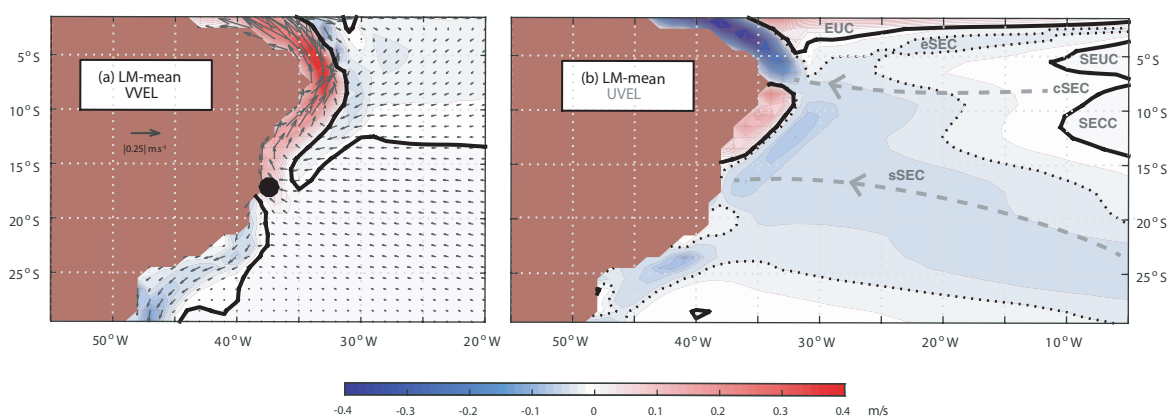


Figure 2. LM-mean South Atlantic Ocean (SAO) circulation pattern. Depth-integrated flow over the upper 200 m for the LM (850–1849): (a) Zonal and meridional velocities (UVEL, VVEL, respectively, as vectors) superposed on the meridional velocities (background colors). Red (blue) denotes positive, northward (negative, southward) velocities. Black contours mark the zero meridional velocity line, and the black dot represents the mean sSEC bifurcation latitude (SBL) at 25 m. (b) Zonal velocities (background colors). Red (blue) denotes positive, eastward (negative, westward) velocities. Black filled contours mark the zero zonal velocity line, and black dotted contours mark the -0.02 m/s contour, for reference. Mean zonal currents from south to north are: the southern branch of the South Equatorial Current (sSEC), the South Equatorial Countercurrent (SECC), the central branch of the South Equatorial Current (cSEC), the South Equatorial Undercurrent (SEUC), the equatorial branch of the South Equatorial Current (eSEC), and the Equatorial Undercurrent (EUC). Gray dashed lines indicate the sSEC and cSEC direction, for reference.

The sSEC is the southernmost westward-flowing branch across the SAO that represents the extension of the BeC and the northern boundary of the SASG [62–64]. It was described by Molinari [65] as the flow south of the SECC and by Stramma [63] as the flow between 10° – 25° S, east of 30° W. This is the branch in which we were interested.

Because the Coriolis force acts favoring the western intensification in subtropical gyre dynamics [66], eastern boundary currents such as the BeC are portrayed as broad and diffuse flows. As a consequence, the resulting gyre’s shape in the x-y plane can be roughly described by a “D-like” format, rather than circular. Thus, the BeC gradually turns northwestward into the sSEC, by following the counter-clockwise SASG circulation. The sSEC in turn crosses the basin and bifurcates as it approaches the SA coast. The sSEC bifurcation region is the latitudinal band where both WBCs begin to form and diverge. This is nearly between 10° – 20° S, around the region of zero meridional velocity (black contour marking the transition between red and blue background interiors in Figure 2a). Part of

the sSEC inflow supplies the eastward flow of the SECC east of 30° W, while most of the sSEC inflow contributes to the NBUC, and only the southern part of the sSEC turns south into the BC [64].

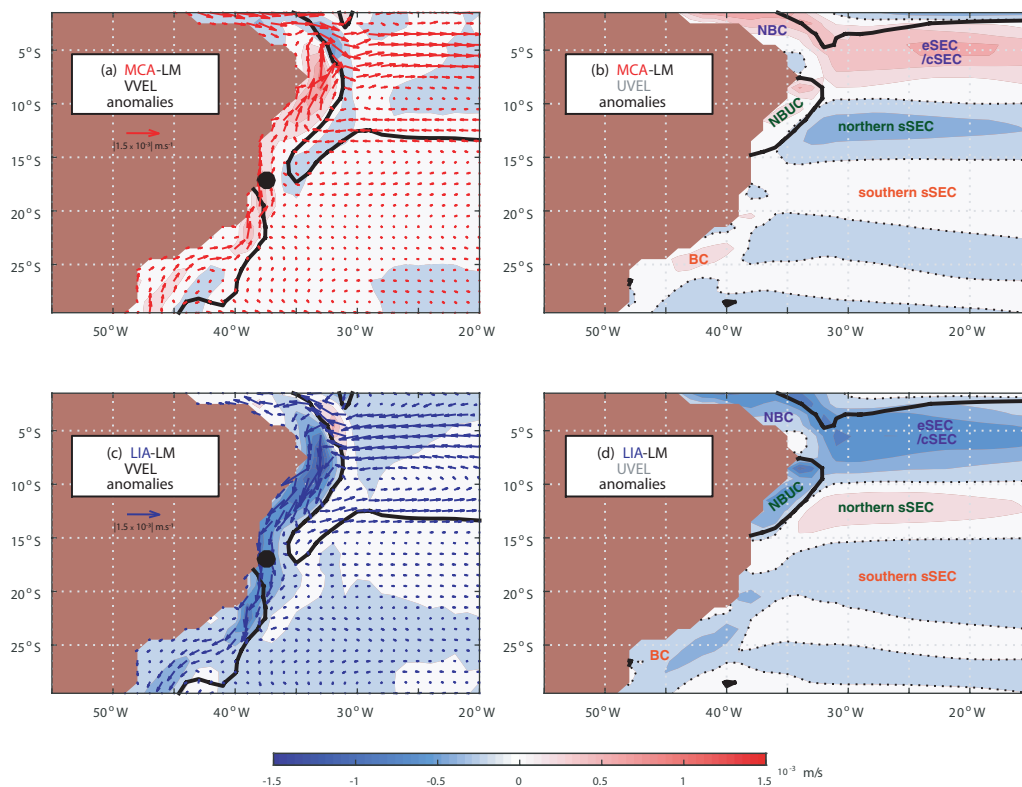


Figure 3. MCA and LIA anomalous SAO circulation pattern. Depth-integrated anomalous flows over the upper 200 m for the (a,b) MCA (950–1249) and (c,d) LIA (1400–1699) periods. (a,c) Anomalous horizontal velocities (UVEL, VVEL, as vectors) superposed on the anomalous meridional velocities (VVEL, background colors). Red (blue) background colors denote positive, northward (negative, southward) anomalies. Black contours mark the LM-mean zero meridional velocity line, for reference, and the black dot represents the MCA/LIA-mean SBL at 25 m. (b,d) Anomalous zonal velocities (UVEL, background colors). Red (blue) background colors denote positive, eastward (negative, westward) anomalies. Black contours mark the LM-mean zero zonal velocity line, for reference. Indicated are the westward basin-wide currents (eSEC/cSEC, northern and southern sSEC) and western boundary currents (North Brazil Current (NBC), North Brazil Undercurrent (NBUC), and Brazil Current (BC)), identified in different colors according to their respective anomalous signals.

3.2.2. MCA and LIA Anomalous Circulation Field

To explore the changes in the western SAO circulation field between the MCA and LIA, we analyzed each of their anomalous horizontal flow fields relative to the whole LM integration (850–1849). Background colors in Figure 3 display the meridional velocity (VVEL, Figure 3a,c) and zonal velocity (UVEL, Figure 3b,d) anomalies for the MCA (Figures 3a,b) and LIA (Figures 3c,d). As in Figure 2a, the superposed vectors over the meridional velocities in Figure 3a (Figure 3c) are the MCA (LIA) anomalous horizontal velocities, highlighting the western boundary anomalies.

Results show clear opposing MCA/LIA anomalous circulation patterns: the MCA was characterized by overall positive VVEL anomalies off the western boundary (Figure 3a), indicating an intensification of the northward NBUC and weakening of the southward BC; while the LIA was subject to overall negative anomalous flows along the coast (Figure 3c) pointing to an NBUC weakening and BC intensification. This means that the inflow carried by the BeC-sSEC system was being directed mostly northward during the MCA and southward during the LIA.

During the MCA, the increase (decrease) in the NBUC (BC) transport caused the SBL to occur slightly in southerly positions (with an MCA-mean SBL of 17.14° S at 25 m (dark dot in Figure 3a)). On the other hand, the opposite is observed in Figure 3c (with a LIA-mean SBL of 17.00° S at 25 m).

The difference between the MCA-mean and the LIA-mean SBL position is therefore of 0.14° latitude. It is a small difference compared to the model resolution ($1^{\circ} \times 1^{\circ}$); nevertheless, considering that the low-passed SBL time series for the 850–1849 total period (whose anomaly time series is displayed in Figure 4a) ranges only from 16.9° – 17.2° S at 25 m, with a standard deviation of 0.09° , this 0.14° difference in position between both periods is considerable. The time series in Figure 4a,b provide the LM-perspective, which evidences the occurrence of a southern (northern) SBL during the MCA (LIA) both near the surface, at 25 m, and at 100 m.

The SST MCA-anomalies shown in Figure 1a reflect this intensification of the AMOC upper limb at this portion: as more warm waters were being transported northward, the BeC-northern sSEC path along the subtropical gyre was marked with greater positive-SST anomalies. In other words, this northwestward, hook-like extension of the positive-SST anomalies agreed with the northward intensification of the flow off the SA coast and southerly SBL position during the MCA as opposed to the LIA.

When looking at the time series of the westward sSEC transport between 9.5° – 24.5° S across 30° W, according to Stramma [63] (Figure 4c, herein referred to as "Total sSEC"), one can conclude that it did not change substantially between the MCA (mean 15.97 Sverdrups (Sv), $1 \text{ Sv} = 10^6 \text{ m}^3 \text{ s}^{-1}$) and the LIA (mean 15.92 Sv). Only by the end of the LIA period, between 1600 and 1700, the transport anomaly fell further below the zero line (lowering the LIA-mean transport value), returning to a highly positive state right afterwards. Except for that episode, the westward transport anomalies fluctuated nearly around the zero line (± 0.06 Sv standard deviation).

Even though the magnitude of the total westward SEC transport remained roughly the same between both the MCA and LIA periods, the zonal velocities varied differently across latitudinal bands within this 9.5° – 24.5° S band, according to the different SEC branches (Figures 3b,d). In these panels, the westward currents crossing the basin and the WBCs fed by those can be associated according to the banded anomalous flow pattern displayed. These regional patterns of the anomalous zonal velocities elucidated how the westward flow was meridionally distributed throughout the coast between the MCA and LIA, considering that the WBCs' meridional flows straddling the SBL have also a zonal component that follows the coastline orientation. Blue shading denotes negative anomalies, which means an intensification of the mean westward flow, while red shading denotes positive anomalies, which imply a weakening of the mean westward flow at the region.

The zonal band of UVEL anomalies between approximately 16.5° S and 19.5° S, which we refer to as southern sSEC, seemed to be related to the poleward flowing BC, in which both their anomalies assumed positive values in the MCA, suggesting a weakening of the southern sSEC-BC system, and negative values during the LIA, suggesting in turn an intensification of the system. This can be interpreted as a decrease (increase) of the SASG circulation in its northwestern boundary during the MCA (LIA). Note that the coastline causes the southward BC flow to continue in the westward direction, and this is why both these currents present anomalies of the same sign.

To the north, the zonal band of UVEL anomalies between approximately 9.5° S and 15.5° S is defined as the northern sSEC. This portion seems to be contributing directly to the NBUC. The northern sSEC-NBUC system appeared to be anomalously strong during the MCA and anomalously weak during the LIA. It should be noted that the NBUC transport assumes a northeastward orientation at this region due to the coastline. As a result, for the MCA (LIA), the negative (positive) anomalies of the northern sSEC fed into the positive (negative) zonal anomalies of the NBUC. This points to more (less) waters being directed towards the Equator and the Northern Hemisphere after the sSEC bifurcation during the MCA (LIA).

The regional patterns of the anomalous flow described above suggest an explanation of how the north-south sSEC distribution occurred between the NBUC and the BC with respect to the warm-MCA

and cold-LIA periods. By entering the tropical system, north of 10° S, the strong band of zonal anomalies observed between approximately 3.5° S and 8.5° S (i.e., the anomalous band straddling 5° S) represents the inflow of the cSEC and possibly part of the eSEC to the western boundary. These override the NBUC north of $\sim 5^{\circ}$ S, from where it turns from an undercurrent to a surface intensified current: the North Brazil Current (NBC) [67]. Therefore, we suggest that the cSEC/eSEC anomalies are related to the NBC anomalies observed north of 3.5° S. They were of opposing sign to the northern sSEC-NBUC anomalies, characterizing a weakened cSEC/eSEC-NBC system during the MCA and an intensified one during the LIA.

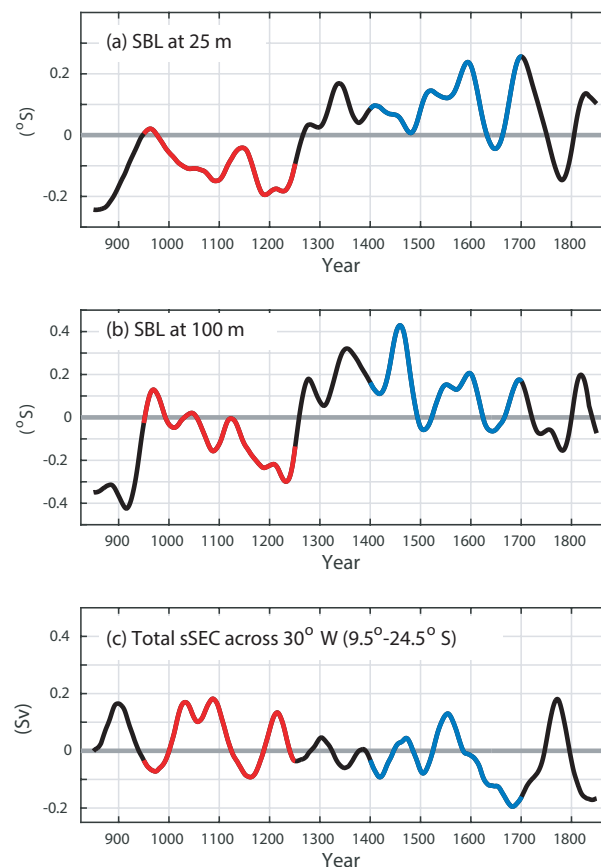


Figure 4. SBL and total sSEC time series. Low-passed (30-year), standardized anomalies of the SBL at 25 m (a) and at 100 m (b) and of the total westward sSEC transport across 30° W, between 9.5° S and 24.5° S and above 200 m (c). The MCA period is marked in red, while the LIA is marked in blue.

Despite the opposing cSEC/eSEC-NBC anomalies with respect to the northern sSEC-NBUC anomalies, what mostly matters for this study is the division of interocean waters carried by the BeC-sSEC between the NBUC and BC circulation regimes. The cSEC actually derives from sSEC recirculation in part [68] and then joins the western boundary around 5° S, transforming the NBUC in the surface-intensified NBC [69]. This suggests that the high-latitude interocean waters are essentially carried by the sSEC prior to feeding any of its branched systems (i.e., BC, NBUC, cSEC). North of the NBUC, the flow might independently be subject to other external forcings; regardless of that, it has already been sent to the north after the sSEC bifurcation.

We suggest that the band of anomalies south of the southern sSEC, between 20.5° S and 24.5° S, is contributing both to the BC and to interior recirculation. The southern sSEC was considered to

be between 16.5° and 19.5° S based on the spatial distribution of its MCA/LIA anomalous signals across 30° W, which correspond to the BC signal, in both the MCA and LIA cases. The distribution of the zonal flow along the coast based on the horizontal anomalies described in Figure 3 was further confirmed by obtaining the volume transport time series. Figure 5 displays the 850–1849 anomalous volume transport time series derived from the horizontal velocity field. The MCA (LIA) period is highlighted in red (blue).

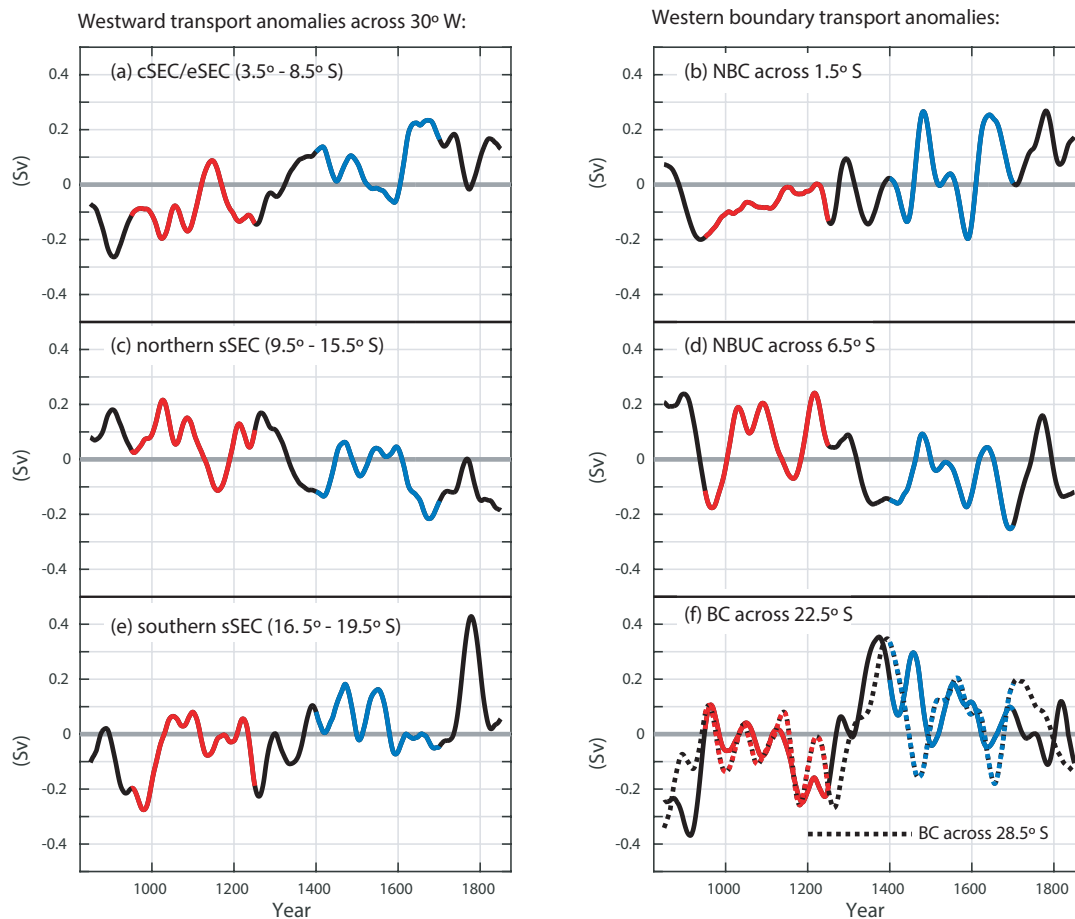


Figure 5. Horizontal volume transport anomalies time series. Low-passed (30-year), standardized anomalies time series of the volume transports above 200 m. (Left column) Westward transports across 30° W at different latitudinal bands from north to south: (a) cSEC/eSEC between 3.5° S and 8.5° S, (c) northern sSEC between 9.5° S and 15.5° S, and (e) southern sSEC between 16.5° S and 19.5° S. (Right column) Western boundary transports fed by the westward transports: (b) northward NBC across 1.5° S, (d) northward NBUC transport across 6.5° S (solid lines) and the basin-integrated MOC streamfunction across the same latitude (dashed lines), and (f) southward BC transport across 22.5° S (solid lines) and across 28.5° S (dashed lines). The MCA period is marked in red, while the LIA is marked in blue.

The time series from Figure 5a–f display an overall similar pattern, especially with respect to their anomalous MCA/LIA signal, supporting our hypothesis that the meridional flow at the western boundary is fed by specific portions of the westward flow coming across the basin. The near-equatorial cSEC/eSEC-NBC system was weaker during the MCA, whilst stronger during the LIA, as well as the southern sSEC-BC system; and the northern sSEC-NBUC system was in turn stronger during the MCA and weaker during the LIA.

Table 1 lists the mean and standard deviation values of the SBL and the volume transports, for the LM, MCA, and LIA periods, corresponding to the time series in Figures 4 and 5. Even though MCA-mean and LIA-mean magnitudes seemed quite similar, their associated anomalies had opposite directions in all cases, as shown in Figure 3b,d.

Table 1. LM-mean and standard deviation (std) and MCA/LIA anomalies (MCA-anom., LIA-anom., with respect to the LM-mean) and std (relative to their 300-year intervals) corresponding to the SBL time series in Figure 4a,b and the volume transport time series in Figures 4c and 5a–f. The total sSEC, cSEC/eSEC, northern sSEC, and southern sSEC transports are across 30° W. Statistically-significant MCA/LIA anomalies are marked in bold, while non-significant ones appear in gray, according to Table 2.

Time Series	LM-Mean ± std	MCA-Anom. ± std	LIA-Anom. ± std
SBL at 25 m	17.07° ± 0.09° S	+0.07° ± 0.04° S	−0.07° ± 0.05° S
SBL at 100 m	20.46° ± 0.04° S	+0.02° ± 0.02° S	−0.03° ± 0.03° S
total sSEC (9.5°–24.5° S)	15.94 ± 0.06 Sv	+0.02 ± 0.05 Sv	−0.02 ± 0.05 Sv
cSEC/eSEC (3.5°–8.5° S)	6.71 ± 0.09 Sv	−0.06 ± 0.05 Sv	+0.06 ± 0.07 Sv
NBC across 1.5° S	13.97 ± 0.05 Sv	−0.03 ± 0.02 Sv	+0.03 ± 0.04 Sv
northern sSEC (9.5°–15.5° S)	8.76 ± 0.06 Sv	+0.03 ± 0.04 Sv	−0.03 ± 0.04 Sv
NBUC across 6.5° S	20.48 ± 0.07 Sv	+0.03 ± 0.06 Sv	−0.04 ± 0.05 Sv
southern sSEC (16.5°–19.5° S)	3.94 ± 0.02 Sv	−0.01 ± 0.02 Sv	+0.01 ± 0.01 Sv
BC across 22.5° S	2.88 ± 0.04 Sv	−0.02 ± 0.02 Sv	+0.02 ± 0.02 Sv
BC across 28.5° S	5.12 ± 0.04 Sv	−0.01 ± 0.02 Sv	+0.02 ± 0.03 Sv

Table 2. Two-sided *t*-test values (*p* < 0.05) between the MCA/LIA and the LM intervals. The significance test was performed between time series of the monthly anomalies, with no low-pass filtering. *p*-values smaller than the 0.05 significance level (i.e., *H* = 1) are marked in bold, while *p*-values greater than 0.05 (i.e., *H* = 0) appear in gray.

Time Series	MCA-LM <i>p</i> -Value	LIA-LM <i>p</i> -Value
SBL at 25 m	1.06 × 10^{−7}	1.19 × 10^{−7}
SBL at 100 m	2.18 × 10^{−6}	2.04 × 10^{−10}
total sSEC (9.5°–24.5° S)	0.0992	0.0244
cSEC/eSEC (3.5°–8.5° S)	8.07 × 10^{−5}	2.68 × 10^{−6}
NBC across 1.5° S	6.63 × 10^{−4}	8.84 × 10^{−6}
northern sSEC (9.5°–15.5° S)	0.0150	0.0043
NBUC across 6.5° S	0.0076	1.63 × 10^{−4}
southern sSEC (16.5°–19.5° S)	0.0448	0.0860
BC across 22.5° S	0.0011	2.11 × 10^{−6}
BC across 28.5° S	0.0091	0.0014

3.3. Wind Stress Curl Field

The wind field distribution also confirmed the observed differences in the SAO circulation pattern between the MCA and LIA (Figure 6). The wind stress is a driving agent of ocean currents, but it is the horizontal gradient rather than the absolute strength that mostly matters: the large-scale wind stress curl, which is, in general, the major forcing mechanism of the upper ocean [61,70]. Positive, anticyclonic WSC provides the torque that drives the SASG circulation.

The WSC anomalies for the MCA are shown in Figure 6a. Predominantly negative anomalies at the region of positive WSC, south of the zero WSC line, pointed to a weakened subtropical gyre circulation. North of the zero WSC line, the negative anomalies suggested an intensification of the cyclonic circulation in the region, which is consistent with the strengthening of the northern sSEC, which feeds into the NBUC (Figures 3b and 5c,d).

For the LIA, Figure 6b shows positive WSC anomalies roughly along the path of the SASG boundary currents (BeC-sSEC-BC-SAC), reinforcing the local positive WSC and strengthening the

subtropical gyre circulation. North of the zero WSC line, the positive WSC anomalies relate to a weakened northern sSEC, instead.

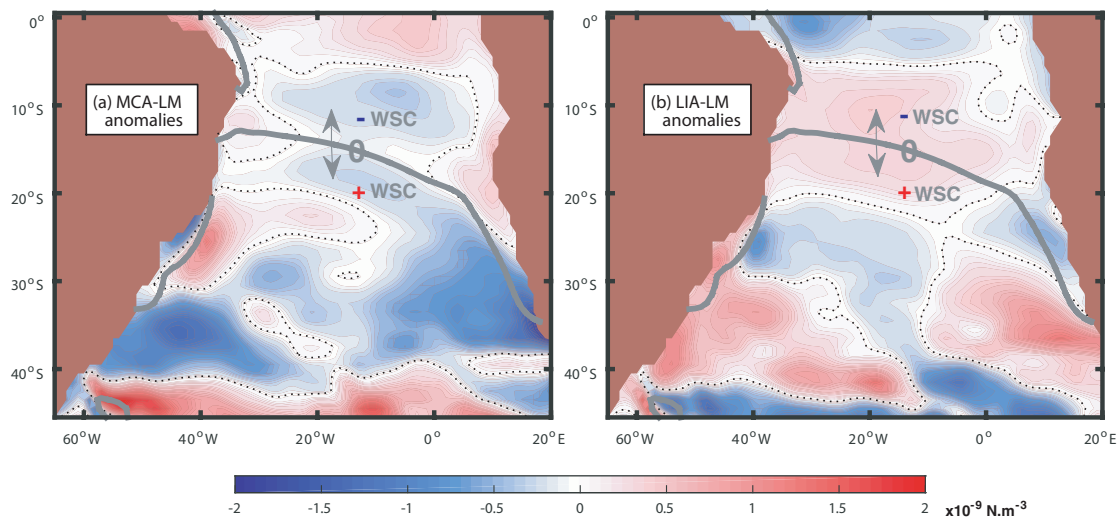


Figure 6. Wind stress curl (WSC) anomalies ($\times 10^{-9} \text{ N}\cdot\text{m}^{-3}$) with respect to the whole-LM base period (850–1849). (a) For the MCA, between 950 and 1249, and (b) for the LIA, between 1400 and 1699. The black dashed contours mark the division between positive (red) and negative (blue) anomalies. The gray solid line denotes the LM-mean zero wind stress curl line, north (south) of which the WSC is negative (positive), i.e., cyclonic (anticyclonic).

4. Discussion and Conclusions

The circulation pattern associated with the South Atlantic surface boundary current system was investigated for the LM, focusing on its response to the warm-MCA and the cold-LIA periods. We examined the along-coast distribution of the sSEC westward flow coming across the SAO basin and bifurcating between the downstream northern and southern circulation regimes. Through the simulation results from the CESM-LME experiment, signals in the SST field suggested a more persistent and far-reaching northward propagation of anomalies along the boundary currents' path during the MCA when compared to the LIA. The circulation field derived from the horizontal velocities revealed overall northward anomalies off the SA coast during the MCA, with increased northern sSEC and NBUC transports, and southward anomalies during the LIA, with increased southern sSEC and BC transports. The SBL accompanies these changes in WBCs transport, as these have an indirect relationship: during the MCA (LIA), the increased northward NBUC (southward BC) transport pushed the SBL to the south (north). Moreover, wind field anomalies indicated that the anticyclonic subtropical WSC, which drives the SASG circulation, was in general weaker during the MCA, while stronger during the LIA.

Together, these results yield a contrasting scenario between the LM-warm and -cold periods. While during the MCA, the flow arriving at the western boundary was preferably directed northward within the AMOC upper limb, during the LIA, a more vigorous SASG circulation was observed, with the increased southward transport.

The MCA/LIA circulation differences described here were in agreement with other large-scale changes reported in the literature for these anomalous periods. During the MCA, the increased northward-NBUC transport and southerly SBL related to studies that pointed to an enhanced AMOC [42] and northern Intertropical Convergence Zone (ITCZ) [71]; while during the LIA, the increased southward-BC transport and northerly SBL provided compelling evidence for a weaker [44] and more saline [72] Gulf Stream, which acted to stabilize the North Atlantic Deep Water

formation [73–75], leading to a weakened AMOC [43], with reduced heat transport and southerly ITCZ [71,72]. The position of the ITCZ responds to meridionally-asymmetrical heating changes, shifting toward the warmer hemisphere [53,76], so that reduced northward surface heat transport cools the North Atlantic relative to the South Atlantic, resulting in increased surface pressure over the North Atlantic and a southward shift of the ITCZ [77].

Even though one might intuitively expect a stronger AMOC taking place since the Twentieth Century warming, in analogy to the warm-MCA period, studies suggested that the AMOC has weakened substantially over the past decades [78] and even the past century, displaying a 1975–present decline trend that is unprecedented in the whole LM [79]. It has been suggested that this weakening occurred as an abrupt shift towards the end of the LIA or as a more gradual decline over the past 150 years [80]. The possible reasons why the AMOC has not swung back to usual warm-intensified conditions instead of continuing to decline after the LIA are still subject to investigation.

Mann et al. [19], Juckes et al. [81], and Ljungqvist et al. [82] agreed that in general, the warmest temperatures of the past millennium occurred around the 11th Century, and the coolest at some point during the 16th–19th Centuries. The MCA and LIA are well marked in proxy records, but reliable only for the Northern Hemisphere [19,24,81–85]. Therefore, there is much to be uncovered about the behavior of the Southern Hemisphere, in particular the South Atlantic Ocean, during these two climatic periods. Very little is known about the Southern Hemisphere climate in the LM, and still, the existing knowledge is over continental regions.

The LM was a stable period, and on average, the magnitude of variations was small. Actually, the coupled ocean response in the South Atlantic for the LM had no apparent trends, although it was sensitive to the warm and cold climate oscillations of the MCA and the LIA.

The western boundary current system off the SA coast is a key region for diagnosing variations of the AMOC and the SASG. Anomalies generated around the southern boundary of the SASG, for example, are advected equatorward through SAO boundary currents up to the SA coast, where the flow is then distributed between both of these circulation regimes. Therefore, the sSEC bifurcation region is a crucial point that separates the large-scale subtropical and meridional overturning circulations.

The AMOC sets the characteristics of the climate system at decadal and longer time scales through its heat and freshwater transports [86], and the SAO provides the gateway by which the AMOC connects with the global ocean. In view of that, being able to associate past climate extremes with changes in SAO circulation pathways is necessary for improved understanding of the range of possible future climate changes at the basin-scale. As climate change extends far beyond the rise in global mean temperatures, the results presented here propose possible responses of the SAO surface boundary current system to abrupt climatic variations.

Supplementary Materials: The following are available online at <http://www.mdpi.com/2076-3263/9/7/299/s1>, Figure S1: Scaled comparison of Figure 2 from Stramma and England [10] with Figure 2b in this study; Figure S2: sSEC bifurcation vertical profile from reanalysis products and model results; Table S1 : Time period, horizontal resolution and number of vertical layers above 1000 m of the 5 ocean reanalysis products used for comparison; Table S2: SBL values obtained by Rodrigues et al. [12] from hydrographic observations, derived from ocean reanalysis products and obtained from the CESM-models results.

Author Contributions: Conceptualization, F.M., I.W.; Data curation, F.M., I.W., B.L.O.-B., E.C.B.; Formal analysis, F.M.; Funding acquisition, F.M., I.W.; Investigation, F.M., I.W., P.R.G.; Methodology, F.M., I.W.; Project administration, F.M.; Resources, I.W.; Software, F.M.; Supervision, I.W.; Validation, F.M.; Visualization, F.M.; Writing—original draft, F.M.; Writing—review & editing, F.M., I.W., P.R.G., B.L.O.-B., E.C.B.

Funding: This study was financed in part by Grants FAPESP 2015/17659-0, 2017/16511-5, CNPq-301726/2013-2, and CNPq-405869/2013-4 and Coordenação de Aperfeiçoamento de Pessoal de Nível Superior, Brasil (CAPES), Finance Code 001.

Acknowledgments: The CESM project is supported primarily by the National Science Foundation (NSF). This material is based on work supported by the National Center for Atmospheric Research (NCAR), which is a major facility sponsored by the NSF under Cooperative Agreement No. 1852977. Computing and data storage resources, including the Cheyenne supercomputer (doi:10.5065/D6RX99HX), were provided by the Computational and Information Systems Laboratory (CISL) at NCAR. Two anonymous journal reviewers are thanked for their comments and suggestions that helped to improve the manuscript.

Conflicts of Interest: The authors declare no conflict of interest.

Abbreviations

The following abbreviations are used in this manuscript:

LM	Last Millennium
MCA	Medieval Climate Anomaly
LIA	Little Ice Age
CESM-LME	Community Earth System Model Last Millennium Ensemble (experiment)
SAO	South Atlantic Ocean
SA	South America (coast)
SASG	South Atlantic Subtropical Gyre
SEC	South Equatorial Current
cSEC	central branch of the SEC
eSEC	equatorial branch of the SEC
sSEC	southern branch of the SEC
SBL	sSEC bifurcation latitude
NBUC	North Brazil Undercurrent
NBC	North Brazil Current
BC	Brazil Current
SAC	South Atlantic Current
EUC	Equatorial Undercurrent
SEUC	South Equatorial Undercurrent
SECC	South Equatorial Countercurrent
MOC	Meridional Overturning Circulation
AMOC	Atlantic MOC
SST	sea surface temperature
VVEL	meridional velocities
UVEL	zonal velocities
WBC	western boundary current
WSC	wind stress curl
ITCZ	Intertropical Convergence Zone
Sv	Sverdrups

References

1. Garzoli, S.; Matano, R. The South Atlantic and the Atlantic meridional overturning circulation. *Deep Sea Res. Part II Top. Stud. Oceanogr.* **2011**, *58*, 1837–1847. [[CrossRef](#)]
2. Rintoul, S.R. South Atlantic interbasin exchange. *J. Geophys. Res. Oceans* **1991**, *96*, 2675–2692. [[CrossRef](#)]
3. Gordon, A.L. Indian-Atlantic transfer of thermocline water at the Agulhas retroflection. *Science* **1985**, *227*, 1030–1033. [[CrossRef](#)] [[PubMed](#)]
4. Talley, L.D. Shallow, Intermediate, and Deep Overturning Components of the Global Heat Budget. *J. Phys. Oceanogr.* **2003**, *33*, 530–560. [[CrossRef](#)]
5. Ganachaud, A. Large-scale mass transports, water mass formation, and diffusivities estimated from World Ocean Circulation Experiment (WOCE) hydrographic data. *J. Geophys. Res.* **2003**, *108*. [[CrossRef](#)]
6. Lumpkin, R.; Speer, K. Large-Scale Vertical and Horizontal Circulation in the North Atlantic Ocean. *J. Phys. Oceanogr.* **2003**, *33*, 1902–1920. [[CrossRef](#)]
7. McCreary, J.P.; Lu, P. Interaction between the Subtropical and Equatorial Ocean Circulations: The Subtropical Cell. *J. Phys. Oceanogr.* **1994**, *24*, 466–497. [[CrossRef](#)]

8. Malanotte-Rizzoli, P.; Hedstromb, K.; Arango, H.; Haidvogel, D.B. Water mass pathways between the subtropical and tropical ocean in a climatological simulation of the North Atlantic ocean circulation. *Dyn. Atmos. Oceans* **2000**, *32*, 331–371. [[CrossRef](#)]
9. Zhang, D.; McPhaden, M.J.; Johns, W.E. Observational Evidence for Flow between the Subtropical and Tropical Atlantic: The Atlantic Subtropical Cells. *J. Phys. Oceanogr.* **2003**, *33*, 1783–1797. [[CrossRef](#)]
10. Stramma, L.; England, M.H. On the water masses and mean circulation of the South Atlantic Ocean. *J. Geophys. Res. Ocean.* **1999**, *104*, 20863–20883. [[CrossRef](#)]
11. Wienders, N.; Arhan, M.; Mercier, H. Circulation at the western boundary of the South and Equatorial Atlantic: Exchanges with the ocean interior. *J. Mar. Res.* **2000**, *58*, 1007–1039. [[CrossRef](#)]
12. Rodrigues, R.R.; Rothstein, L.M.; Wimbush, M. Seasonal Variability of the South Equatorial Current Bifurcation in the Atlantic Ocean: A Numerical Study. *J. Phys. Oceanogr.* **2007**, *37*, 16–30. [[CrossRef](#)]
13. Marcello, F.; Wainer, I.; Rodrigues, R.R. South Atlantic Subtropical Gyre late twentieth century changes. *J. Geophys. Res. Oceans* **2018**, *123*. [[CrossRef](#)]
14. Smeed, D.; Josey, S.; Beaulieu, C.; Johns, W.; Moat, B.; Frajka-Williams, E.; Rayner, D.; Meinen, C.; Baringer, M.; Bryden, H.; et al. The North Atlantic Ocean is in a state of reduced overturning. *Geophys. Res. Lett.* **2018**, *45*, 1527–1533. [[CrossRef](#)]
15. Masson-Delmotte, V.; Schulz, M.; Abe-Ouchi, A.; Beer, J.; Ganopolski, A.; González Rouco, J.; Jansen, E.; Lambeck, K.; Luterbacher, J.; Naish, T.; et al. Information from paleoclimate archives. *Clim. Chang.* **2013**. [[CrossRef](#)]
16. Schmidt, G.A.; Shindell, D.T.; Tsigaridis, K. Reconciling warming trends. *Nat. Geosci.* **2014**, *7*, 158. [[CrossRef](#)]
17. Atwood, A.; Wu, E.; Frierson, D.; Battisti, D.; Sachs, J. Quantifying climate forcings and feedbacks over the last millennium in the CMIP5–PMIP3 models. *J. Clim.* **2016**, *29*, 1161–1178. [[CrossRef](#)]
18. Barnett, T.; Zwiers, F.; Hengerl, G.; Allen, M.; Crowley, T.; Gillett, N.; Hasselmann, K.; Jones, P.; Santer, B.; Schnur, R.; et al. Detecting and attributing external influences on the climate system: A review of recent advances. *J. Clim.* **2005**, *18*, 1291–1314. [[CrossRef](#)]
19. Mann, M.E.; Zhang, Z.; Rutherford, S.; Bradley, R.S.; Hughes, M.K.; Shindell, D.; Ammann, C.; Faluvegi, G.; Ni, F. Global Signatures and Dynamical Origins of the Little Ice Age and Medieval Climate Anomaly. *Science* **2009**, *326*, 1256. [[CrossRef](#)]
20. Jones, P.D.; Mann, M.E. Climate over past millennia. *Rev. Geophys.* **2004**, *42*, RG2002. [[CrossRef](#)]
21. Bradley, R.S.; Briffa, K.R.; Cole, J.; Hughes, M.K.; Osborn, T.J. The climate of the last millennium. In *Paleoclimate, Global Change and the Future*; Springer: Cham, Switzerland, 2003; pp. 105–141.
22. Diaz, H.F.; Trigo, R.; Hughes, M.K.; Mann, M.E.; Xoplaki, E.; Barriopedro, D. Spatial and temporal characteristics of climate in medieval times revisited. *Bull. Am. Meteorol. Soc.* **2011**, *92*, 1487–1500. [[CrossRef](#)]
23. PAGES 2k Consortium. Continental-scale temperature variability during the past two millennia. *Nat. Geosci.* **2013**, *6*, 339. [[CrossRef](#)]
24. IPCC Climate Change: The Physical Science Basis. In *Contribution of Working Group I to the Fourth Assessment Report of the Intergovernmental Panel on Climate Change*; IPCC: Geneva, Switzerland, 2007.
25. Fernández-Donado, J.; Raible, C.; Ammann, C.; Barriopedro, D.; Garcia-Bustamante, E.; Jungclauss, J.; Lorenz, S.; Luterbacher, J.; Phipps, S.; Servonnat, J.; et al. Large-scale temperature response to external forcing in simulations and reconstructions of the last millennium. *Clim. Past* **2013**, *9*, 393–421. [[CrossRef](#)]
26. Neukom, R.; Gergis, J.; Karoly, D.J.; Wanner, H.; Curran, M.; Elbert, J.; González-Rouco, F.; Linsley, B.K.; Moy, A.D.; Mundo, I.; et al. Inter-hemispheric temperature variability over the past millennium. *Nat. Clim. Chang.* **2014**, *4*, 362. [[CrossRef](#)]
27. Le, T.; Sjolte, J.; Muscheler, R. The influence of external forcing on subdecadal variability of regional surface temperature in CMIP5 simulations of the last millennium. *J. Geophys. Res. Atmos.* **2016**, *121*, 1671–1682. [[CrossRef](#)]
28. Cheung, A.H.; Mann, M.E.; Steinman, B.A.; Frankcombe, L.M.; England, M.H.; Miller, S.K. Comparison of low-frequency internal climate variability in CMIP5 models and observations. *J. Clim.* **2017**, *30*, 4763–4776. [[CrossRef](#)]
29. Coats, S.; Smerdon, J.E. Climate variability: The Atlantic’s internal drum beat. *Nat. Geosci.* **2017**, *10*, 470. [[CrossRef](#)]

30. Wang, J.; Yang, B.; Ljungqvist, F.C.; Luterbacher, J.; Osborn, T.J.; Briffa, K.R.; Zorita, E. Internal and external forcing of multidecadal Atlantic climate variability over the past 1200 years. *Nat. Geosci.* **2017**, *10*, 512. [[CrossRef](#)]
31. Ljungqvist, F.C.; Zhang, Q.; Brattström, G.; Krusic, P.J.; Seim, A.; Li, Q.; Zhang, Q.; Moberg, A. Centennial-scale temperature change in last millennium simulations and proxy-based reconstructions. *J. Clim.* **2019**, *32*, 2441–2482. [[CrossRef](#)]
32. Graham, N.; Ammann, C.; Fleitmann, D.; Cobb, K.; Luterbacher, J. Support for global climate reorganization during the Medieval Climate Anomaly. *Clim. Dyn.* **2011**, *37*, 1217–1245. [[CrossRef](#)]
33. Crowley, T.J. Causes of climate change over the past 1000 years. *Science* **2000**, *289*, 270–277. [[CrossRef](#)]
34. Gray, L.J.; Beer, J.; Geller, M.; Haigh, J.D.; Lockwood, M.; Matthes, K.; Cubasch, U.; Fleitmann, D.; Harrison, G.; Hood, L.; et al. Solar influences on climate. *Rev. Geophys.* **2010**, *48*. [[CrossRef](#)]
35. Meehl, G.A.; Arblaster, J.M.; Branstator, G.; Van Loon, H. A coupled air–sea response mechanism to solar forcing in the Pacific region. *J. Clim.* **2008**, *21*, 2883–2897. [[CrossRef](#)]
36. Meehl, G.A.; Arblaster, J.M.; Matthes, K.; Sassi, F.; van Loon, H. Amplifying the Pacific climate system response to a small 11-year solar cycle forcing. *Science* **2009**, *325*, 1114–1118. [[CrossRef](#)]
37. Kaufman, D.S.; Schneider, D.P.; McKay, N.P.; Ammann, C.M.; Bradley, R.S.; Briffa, K.R.; Miller, G.H.; Otto-Bliesner, B.L.; Overpeck, J.T.; Vinther, B.M.; et al. Recent warming reverses long-term Arctic cooling. *Science* **2009**, *325*, 1236–1239. [[CrossRef](#)]
38. Miller, G.H.; Geirsdóttir, Á.; Zhong, Y.; Larsen, D.J.; Otto-Bliesner, B.L.; Holland, M.M.; Bailey, D.A.; Refsnider, K.A.; Lehman, S.J.; Southon, J.R.; et al. Abrupt onset of the Little Ice Age triggered by volcanism and sustained by sea-ice/ocean feedbacks. *Geophys. Res. Lett.* **2012**, *39*. [[CrossRef](#)]
39. Moreno-Chamarro, E.; Zanchettin, D.; Lohmann, K.; Luterbacher, J.; Jungclauss, J.H. Winter amplification of the European Little Ice Age cooling by the subpolar gyre. *Sci. Rep.* **2017**, *7*, 9981. [[CrossRef](#)]
40. Schmidt, G.A.; Jungclauss, J.; Ammann, C.; Bard, E.; Braconnot, P.; Crowley, T.; Delaygue, G.; Joos, F.; Krivova, N.; Muscheler, R.; et al. Climate forcing reconstructions for use in PMIP simulations of the last millennium (v1. 0). *Geosci. Model Dev.* **2011**, *4*, 33–45. [[CrossRef](#)]
41. Otto-Bliesner, B.L.; Brady, E.C.; Fasullo, J.; Jahn, A.; Landrum, L.; Stevenson, S.; Rosenbloom, N.; Mai, A.; Strand, G. Climate variability and change since 850 C.E.: An ensemble approach with the Community Earth System Model (CESM). *Bull. Am. Meteorol. Soc.* **2015**, *97*, 787–801. [[CrossRef](#)]
42. Trouet, V.; Esper, J.; Graham, N.E.; Baker, A.; Scourse, J.D.; Frank, D.C. Persistent positive North Atlantic Oscillation mode dominated the medieval climate anomaly. *Science* **2009**, *324*, 78–80. [[CrossRef](#)]
43. Trouet, V.; Scourse, J.; Raible, C. North Atlantic storminess and Atlantic Meridional Overturning Circulation during the last Millennium: Reconciling contradictory proxy records of NAO variability. *Glob. Planet. Chang.* **2012**, *84*, 48–55. [[CrossRef](#)]
44. Lund, D.C.; Lynch-Stieglitz, J.; Curry, W.B. Gulf Stream density structure and transport during the past millennium. *Nature* **2006**, *444*, 601. [[CrossRef](#)]
45. Neukom, R.; Luterbacher, J.; Villalba, R.; Küttel, M.; Frank, D.; Jones, P.; Grosjean, M.; Wanner, H.; Aravena, J.C.; Black, D.; et al. Multiproxy summer and winter surface air temperature field reconstructions for southern South America covering the past centuries. *Clim. Dyn.* **2011**, *37*, 35–51. [[CrossRef](#)]
46. Landrum, L.; Otto-Bliesner, B.L.; Wahl, E.R.; Conley, A.; Lawrence, P.J.; Rosenbloom, N.; Teng, H. Last millennium climate and its variability in CCSM4. *J. Clim.* **2013**, *26*, 1085–1111. [[CrossRef](#)]
47. Kay, J.; Deser, C.; Phillips, A.; Mai, A.; Hannay, C.; Strand, G.; Arblaster, J.; Bates, S.; Danabasoglu, G.; Edwards, J.; et al. The Community Earth System Model (CESM) large ensemble project: A community resource for studying climate change in the presence of internal climate variability. *Bull. Am. Meteorol. Soc.* **2015**, *96*, 1333–1349. [[CrossRef](#)]
48. Danabasoglu, G.; Bates, S.C.; Briegleb, B.P.; Jayne, S.R.; Jochum, M.; Large, W.G.; Peacock, S.; Yeager, S.G. The CCSM4 ocean component. *J. Clim.* **2012**, *25*, 1361–1389. [[CrossRef](#)]
49. Wainer, I.; Gent, P.R. Changes in the Atlantic Sector of the Southern Ocean estimated from the CESM Last Millennium Ensemble. *Antarct. Sci.* **2019**, *31*, 37–51. [[CrossRef](#)]
50. Figueiredo Prado, L.; Wainer, I.; Leite da Silva Dias, P. Tropical Atlantic Response to Last Millennium Volcanic Forcing. *Atmosphere* **2018**, *9*, 421. [[CrossRef](#)]

51. Abram, N.J.; McGregor, H.V.; Tierney, J.E.; Evans, M.N.; McKay, N.P.; Kaufman, D.S.; Thirumalai, K.; Martrat, B.; Goosse, H.; Phipps, S.J.; et al. Early onset of industrial-era warming across the oceans and continents. *Nature* **2016**, *536*, 411. [[CrossRef](#)]
52. Huang, W.; Feng, S.; Liu, C.; Chen, J.; Chen, J.; Chen, F. Changes of climate regimes during the last millennium and the twenty-first century simulated by the Community Earth System Model. *Quat. Sci. Rev.* **2018**, *180*, 42–56. [[CrossRef](#)]
53. Stevenson, S.; Otto-Bliesner, B.; Fasullo, J.; Brady, E. “El Niño like” hydroclimate responses to last millennium volcanic eruptions. *J. Clim.* **2016**, *29*, 2907–2921. [[CrossRef](#)]
54. Stevenson, S.; Overpeck, J.T.; Fasullo, J.; Coats, S.; Parsons, L.; Otto-Bliesner, B.; Ault, T.; Loope, G.; Cole, J. Climate variability, volcanic forcing, and last Millennium hydroclimate extremes. *J. Clim.* **2018**, *31*, 4309–4327. [[CrossRef](#)]
55. Zambri, B.; LeGrande, A.N.; Robock, A.; Slawinska, J. Northern Hemisphere winter warming and summer monsoon reduction after volcanic eruptions over the last millennium. *J. Geophys. Res. Atmos.* **2017**, *122*, 7971–7989. [[CrossRef](#)]
56. CESM–LME. Last Millennium Ensemble Publications. Available online: <http://www.cesm.ucar.edu/projects/community-projects/LME/publications.html> (accessed on 26 June 2019).
57. Zhang, X.; Peng, S.; Ciais, P.; Wang, Y.P.; Silver, J.D.; Piao, S.; Rayner, P.J. Greenhouse gas concentration and volcanic eruptions controlled the variability of terrestrial carbon uptake over the last millennium. *J. Adv. Model. Earth Syst.* **2019**. [[CrossRef](#)]
58. Munoz, S.E.; Dee, S.G. El Niño increases the risk of lower Mississippi River flooding. *Sci. Rep.* **2017**, *7*, 1772. [[CrossRef](#)]
59. Deser, C.; Phillips, A.S.; Tomas, R.A.; Okumura, Y.M.; Alexander, M.A.; Capotondi, A.; Scott, J.D.; Kwon, Y.O.; Ohba, M. ENSO and Pacific decadal variability in the Community Climate System Model version 4. *J. Clim.* **2012**, *25*, 2622–2651. [[CrossRef](#)]
60. Ault, T.; Deser, C.; Newman, M.; Emile-Geay, J. Characterizing decadal to centennial variability in the equatorial Pacific during the last millennium. *Geophys. Res. Lett.* **2013**, *40*, 3450–3456. [[CrossRef](#)]
61. Cai, W. Antarctic ozone depletion causes an intensification of the Southern Ocean super-gyre circulation. *Geophys. Res. Lett.* **2006**, *33*. [[CrossRef](#)]
62. Peterson, R.G.; Stramma, L. Upper-level circulation in the South Atlantic Ocean. *Prog. Oceanogr.* **1991**, *26*, 1–73. [[CrossRef](#)]
63. Stramma, L. Geostrophic transport of the South Equatorial Current in the Atlantic. *J. Mar. Res.* **1991**, *49*, 281–294. [[CrossRef](#)]
64. Stramma, L.; Schott, F. The mean flow field of the tropical Atlantic Ocean. *Deep Sea Res. Part II Top. Stud. Oceanogr.* **1999**, *46*, 279–303. [[CrossRef](#)]
65. Molinari, R.L. Observations of eastward currents in the tropical South Atlantic Ocean: 1978–1980. *J. Geophys. Res. Oceans* **1982**, *87*, 9707–9714. [[CrossRef](#)]
66. Stommel, H. The westward intensification of wind-driven ocean currents. *EOS Trans. Am. Geophys. Union* **1948**, *29*, 202–206. [[CrossRef](#)]
67. Schott, F.A.; Stramma, L.; Fischer, J. The warm water inflow into the western tropical Atlantic boundary regime, spring 1994. *J. Geophys. Res. Oceans* **1995**, *100*, 24745–24760. [[CrossRef](#)]
68. Stramma, L.; Schott, F. Western Equatorial Circulation and Interhemispheric Exchange. In *The Warmwatersphere of the North Atlantic Ocean*; Krauss, W., Ed.; Gebrüder Borntraeger: Berlin, Stuttgart, 1996; pp. 195–227.
69. Schott, F.A.; Fischer, J.; Stramma, L. Transports and pathways of the upper-layer circulation in the western tropical Atlantic. *J. Phys. Oceanogr.* **1998**, *28*, 1904–1928. [[CrossRef](#)]
70. Goni, G.J.; Wainer, I. Investigation of the Brazil Current front variability from altimeter data. *J. Geophys. Res. Oceans* **2001**, *106*, 31117–31128. [[CrossRef](#)]
71. Haug, G.H.; Hughen, K.A.; Sigman, D.M.; Peterson, L.C.; Röhl, U. Southward migration of the intertropical convergence zone through the Holocene. *Science* **2001**, *293*, 1304–1308. [[CrossRef](#)]
72. Lund, D.C.; Curry, W. Florida Current surface temperature and salinity variability during the last millennium. *Paleoceanogr. Paleoclimatol.* **2006**, *21*. [[CrossRef](#)]
73. Vellinga, M.; Wood, R.A.; Gregory, J.M. Processes governing the recovery of a perturbed thermohaline circulation in HadCM3. *J. Clim.* **2002**, *15*, 764–780. [[CrossRef](#)]

74. Vellinga, M.; Wu, P. Low-latitude freshwater influence on centennial variability of the Atlantic thermohaline circulation. *J. Clim.* **2004**, *17*, 4498–4511. [[CrossRef](#)]
75. Keigwin, L.; Boyle, E. Detecting Holocene changes in thermohaline circulation. *Proc. Natl. Acad. Sci. USA* **2000**, *97*, 1343–1346. [[CrossRef](#)] [[PubMed](#)]
76. Kang, S.M.; Held, I.M.; Frierson, D.M.; Zhao, M. The response of the ITCZ to extratropical thermal forcing: Idealized slab-ocean experiments with a GCM. *J. Clim.* **2008**, *21*, 3521–3532. [[CrossRef](#)]
77. Hastenrath, S.; Greischar, L. Circulation mechanisms related to northeast Brazil rainfall anomalies. *J. Geophys. Res. Atmos.* **1993**, *98*, 5093–5102. [[CrossRef](#)]
78. Srokosz, M.; Bryden, H. Observing the Atlantic Meridional Overturning Circulation yields a decade of inevitable surprises. *Science* **2015**, *348*, 1255575. [[CrossRef](#)] [[PubMed](#)]
79. Rahmstorf, S.; Box, J.E.; Feulner, G.; Mann, M.E.; Robinson, A.; Rutherford, S.; Schaffernicht, E.J. Exceptional twentieth-century slowdown in Atlantic Ocean overturning circulation. *Nat. Clim. Chang.* **2015**, *5*, 475. [[CrossRef](#)]
80. Thornalley, D.J.; Oppo, D.W.; Ortega, P.; Robson, J.I.; Brierley, C.M.; Davis, R.; Hall, I.R.; Moffa-Sanchez, P.; Rose, N.L.; Spooner, P.T.; et al. Anomalously weak Labrador Sea convection and Atlantic overturning during the past 150 years. *Nature* **2018**, *556*, 227. [[CrossRef](#)] [[PubMed](#)]
81. Juckes, M.N.; Allen, M.R.; Briffa, K.R.; Esper, J.; Hegerl, G.; Moberg, A.; Osborn, T.; Weber, S. Millennial temperature reconstruction intercomparison and evaluation. *Clim. Past* **2007**, *3*, 591–609. [[CrossRef](#)]
82. Ljungqvist, F. A new reconstruction of temperature variability in the extra-tropical Northern Hemisphere during the last two millennia. *Geogr. Ann. A* **2010**, *92*, 339–351. [[CrossRef](#)]
83. Mann, M.E.; Zhang, Z.; Hughes, M.K.; Bradley, R.S.; Miller, S.K.; Rutherford, S.; Ni, F. Proxy-based reconstructions of hemispheric and global surface temperature variations over the past two millennia. *Proc. Natl. Acad. Sci. USA* **2008**, *105*, 13252–13257. [[CrossRef](#)]
84. PAGES 2k-PMIP3 Group. Continental-scale temperature variability in PMIP3 simulations and PAGES 2k regional temperature reconstructions over the past millennium. *Clim. Past* **2015**, *11*, 1673–1699. [[CrossRef](#)]
85. Smerdon, J.; Pollack, H. Reconstructing Earth's surface temperature over the past 2000 years: The science behind the headlines. *Wiley Interdiscip. Rev. Clim. Chang.* **2016**, *7*, 746–771 [[CrossRef](#)]
86. Buckley, M.W.; Marshall, J. Observations, inferences, and mechanisms of the Atlantic Meridional Overturning Circulation: A review. *Rev. Geophys.* **2016**, *54*, 5–63. [[CrossRef](#)]



© 2019 by the authors. Licensee MDPI, Basel, Switzerland. This article is an open access article distributed under the terms and conditions of the Creative Commons Attribution (CC BY) license (<http://creativecommons.org/licenses/by/4.0/>).